

A near-global climatology of oceanic coherent eddies

Josué Martínez-Moreno¹, Andrew McC. Hogg¹, and Matthew H. England²

¹Research School of Earth Science and ARC Center of Excellence for Climate Extremes, Australian National University, Canberra, Australia

²Climate Change Research Centre (CCRC), UNSW Australia, Sydney NSW, Australia

Key Points:

- Coherent eddies contain around 50% of the total surface ocean kinetic energy budget.
- Seasonal cycle of the number of coherent eddies and the coherent eddy amplitude reveals a 3-6 month lag to wind forcing.
- The seasonal lag between the number and the amplitude of coherent eddies suggests a role for the inverse cascade.

13 **Abstract**

14 Ocean eddies influence regional and global climate through mixing and transport of heat
 15 and properties. One of the most recognizable and ubiquitous features of oceanic eddies
 16 are coherent vortices with spatial scales of tens to hundreds of kilometers, frequently re-
 17 ferred as “mesoscale eddies”. Coherent mesoscale eddies are known to transport prop-
 18 erties across the ocean and to locally affect near-surface wind, cloud properties, and rain-
 19 fall patterns. Although coherent eddies are ubiquitous, their climatology, seasonality, and
 20 long-term temporal evolution remains poorly understood. Here, we examine the kinetic
 21 energy contained in coherent eddies and present the seasonal, interannual and long-term
 22 variability using satellite observations between 1993 and 2019. A total of \sim 37 million
 23 coherent eddies are detected in this analysis. Around 50% of the kinetic energy contained
 24 by ocean eddies corresponds to coherent eddies. Additionally, a strong seasonal cycle is
 25 observed, with a 3–6 month lag between the wind forcing and the response of the coher-
 26 ent eddy field. The seasonality of the number of coherent eddies and their amplitude re-
 27 veals that the number of coherent eddies responds faster to the forcing (\sim 3 months), than
 28 the coherent eddy amplitude (which lags by \sim 6 months). This seasonal cycle is spatially
 29 variable, so we also analyze the eddy climatology in key oceanic regions. Our analysis
 30 highlights the relative importance of the coherent eddy field in the ocean kinetic energy
 31 budget, implies a strong response of the eddy number and eddy amplitude to forcing at
 32 different time-scales, and showcases the seasonality, and multidecadal trends of coher-
 33 ent eddy properties.

34 **Plain language summary**35 **Plain summary**

36 Coherent eddies are the most common feature of ocean variability observable from
 37 satellites. They are crucial in ocean dynamics as they can transport properties over long
 38 distances and interact with the atmosphere. Our study investigates the seasonal, inter-
 39 annual, and long-term changes in the abundance and intensity of coherent eddies, by au-
 40 tomatically identifying individual eddies over the available satellite altimeter record. The
 41 seasonal cycle suggests a transition from numerous, smaller, and weaker coherent eddies,
 42 to fewer and larger, and stronger coherent eddies over the season. In addition, a long-
 43 term adjustment of the coherent eddy field is identified with possible links to long-term
 44 changes in the climate system.

45 **1 Introduction**

46 Mesoscale ocean variability with spatial scales of tens to hundreds of kilometers is
47 comprised of processes such as vortices, waves, and jets (Ferrari & Wunsch, 2009; Fu et
48 al., 2010). These mesoscale processes are highly energetic, and they play a crucial role
49 in the transport of heat, salt, momentum, and other tracers through the ocean (Gill et
50 al., 1974; Wyrtki et al., 1976; Wunsch & Ferrari, 2004). One of the most recognizable
51 and abundant ocean processes observable from space are mesoscale vortices. Although
52 mesoscale vortices are commonly referred to in the literature as “mesoscale eddies”, this
53 term is also often used to describe the total mesoscale ocean variability (the time-varying
54 component of the mesoscale flow). Thus, to avoid ambiguity we will refer to mesoscale
55 vortices as *coherent eddies*. Coherent eddies are abundant and energetic; they are essen-
56 tial to ocean dynamics as concluded by many previous studies (Hogg & Blundell, 2006;
57 Siegel et al., 2011; Beron-Vera et al., 2013; Frenger et al., 2013, 2015; Pilo et al., 2015;
58 Schubert et al., 2019; Patel et al., 2020).

59 Coherent eddies are quasi-circular geostrophic currents. According to their rota-
60 tional direction and the sign of the Coriolis parameter, the sea surface height anomaly
61 within a coherent eddy can be negative or positive (cold-core and warm-core coherent
62 eddies, respectively). This characteristic sea surface height signature of coherent eddies
63 has been utilized to identify and track coherent eddies from satellite altimetry (e.g., Chel-
64 ton et al., 2007; Faghmous et al., 2015; Ashkezari et al., 2016; Martínez-Moreno et al.,
65 2019; Cui et al., 2020). Automated algorithms for identification of coherent eddies have
66 revealed their ubiquity in the oceans, with a predominant influence at hotspots of eddy
67 activity such as in boundary current extensions and the Antarctic Circumpolar Current.
68 In these regions, it has been estimated that coherent eddies contribute around 40–50%
69 of the net mesoscale kinetic energy (Chelton et al., 2011) and thus a significant fraction
70 of the total kinetic energy (Ferrari & Wunsch, 2009). Although this estimate showcases
71 the importance of the mesoscale coherent eddy field, the energy contained in coherent
72 eddies was estimated by extracting the total geostrophic velocity within the radius of
73 each detected coherent eddy; thus, it is possible that this estimate may contain energy
74 from other processes. Here we extend on this past work by reconstructing the surface
75 imprint of coherent eddies using a new eddy tracking algorithm and using the latest avail-
76 able satellite record.

77 There is broad consensus that mesoscale eddy kinetic energy has a pronounced sea-
78 sonal variability (Qiu, 1999; Qiu & Chen, 2004; Kang & Curchitser, 2017; Uchida et al.,
79 2017). Several hypotheses have been proposed to explain this seasonality including: sea-
80 sonal variations of atmospheric forcing (Sasaki et al., 2014), seasonality of the mixed layer
81 depth (Qiu et al., 2014; Callies et al., 2015), seasonality of the intensity of barotropic in-
82 stability (Qiu & Chen, 2004), the variability of the baroclinic instability due to the sea-
83 sonality of the vertical shear (Qiu, 1999), and a seasonal lag of the inverse energy cas-
84 cade (i.e. energy is transported between scales, from small to large; Arbic et al., 2013)
85 in combination with the presence of a front in the mixed layer, which can lead to a sea-
86 sonal cycle of the baroclinic instability (Qiu et al., 2014). On one hand, processes such
87 as barotropic and baroclinic instabilities control the seasonality of coherent eddies in the
88 ocean. On the other hand, recent studies using observations and eddy-permitting climate
89 models suggest slower adjustments of the global ocean that create long-term changes in
90 the coherent eddy field. Such readjustments include a multidecadal increase in the ocean
91 stratification resulting from temperature and salinity changes (Li et al., 2020), a hori-
92 zontal readjustment of sea surface temperature gradients (Cane et al., 1997; Bouali et
93 al., 2017; Ruela et al., 2020), and an intensification of the kinetic energy, eddy kinetic
94 energy, and mesoscale eddy kinetic energy over the last 3 decades as a consequence of
95 an increase in wind forcing (Hu et al., 2020; Wunsch, 2020; Martínez-Moreno et al., 2021).
96 All of these seasonal factors and long-term readjustments directly influence the annual
97 and decadal response of the coherent eddy field, however, the seasonality of the coher-
98 ent component of the eddy kinetic energy, as well as the seasonal cycle and trends of the
99 coherent eddy statistics, remain unknown.

100 Here we present a new global climatology of the coherent eddy kinetic energy by
101 reconstructing the coherent eddy signature from satellite observations. Our study doc-
102 uments the seasonal cycle of the coherent eddy kinetic energy, and the seasonal cycle and
103 long-term trends of the coherent eddy properties over the satellite record. Moreover, we
104 conduct more detailed analyses in regions where coherent eddies dominate the eddy ki-
105 netic energy field. The rest of this paper is structured as follows: the data sources and
106 methodology are described in Section 2. Then, we present the climatology, energy ra-
107 tios, and global seasonality of the coherent eddy kinetic energy in Section 3. Section 4
108 outlines the global climatology and seasonality of coherent eddy properties, followed by
109 long-term changes of the coherent eddy properties (Section 5). Then we focus our at-

110 tention on the seasonal cycle and coherent eddy properties in regions dominated by co-
 111 herent eddies (Section 6). Finally, Section 7 summarizes the main results and discusses
 112 the implications of this study.

113 **2 Methods**

114 We use daily [all satellite](#) sea surface height (SSH) data made available by the Coper-
 115 nicus Marine Environment Monitoring Service [in near real time](#) (CMEMS, 2017). This
 116 gridded product contains the sea surface height and geostrophic velocities with daily 0.25°
 117 resolution from January 1993 to December 2019. The daily geostrophic velocities allow
 118 us to compute the kinetic energy (KE) and eddy kinetic energy (EKE) over the satel-
 119 lite record. The [main source of EKE is the time-varying wind](#) [primary source of energy](#)
 120 [in the ocean is exerted by wind stress at the surface](#) (Ferrari & Wunsch, 2009); thus, we
 121 also compute the seasonal cycle of the wind magnitude from the JRA55 reanalysis (Japan
 122 Meteorological Agency, Japan, 2013) using wind velocities at 10m above the ocean's sur-
 123 face.

124 Over the same record, coherent eddy statistics from Martínez-Moreno et al. (2019),
 125 hereafter MM19, are analyzed and compared with those released by Chelton & Schlax
 126 (2013), hereafter CS13. Both datasets are gridded at 1° resolution and are produced via
 127 automated eddy identification algorithms using closed contours of SSH. However, these
 128 datasets have important differences in the criteria they use to identify and record coher-
 129 ent eddy statistics. The major differences include: (i) MM19's algorithm requires an ad-
 130 justment between a 2D Gaussian and the SSH anomaly (SSHa) surface within the iden-
 131 tified closed contour, while CS13's only uses the outermost closed contour of SSH; (ii)
 132 MM19's dataset reports the maximum SSHa within the identified coherent eddy, while
 133 CS13's algorithm reports the maximum SSH value minus the discrete level in which the
 134 coherent eddy was identified; and (iii) MM19's dataset includes all detected coherent ed-
 135 dies, while CS13's dataset excludes coherent eddies with lifetimes shorter than four weeks
 136 and coherent eddy amplitudes smaller than 1cm. Moreover, MM19's algorithm allows
 137 the reconstruction of the coherent eddy field under the assumption that coherent eddies
 138 have a 2D Gaussian imprint in the sea surface height. This Gaussian reconstruction of
 139 the coherent eddy field then allows us to estimate the coherent geostrophic eddy veloc-
 140 ities and thus the kinetic energy contained only in coherent eddies.

141 **2.1 Kinetic Energy decomposition**

142 Kinetic energy is commonly divided into the mean and time-varying components
 143 through a Reynolds decomposition. At a given time, the surface velocity field $\mathbf{u} = (u, v)$
 144 is split into the time mean ($\bar{\mathbf{u}}$) and time varying components (\mathbf{u}'). Moreover, MM19 pro-
 145 posed to further decompose the eddy kinetic energy into the energy of coherent features
 146 (\mathbf{u}'_e) and non-coherent features (\mathbf{u}'_n). Therefore the KE equation can be written as:

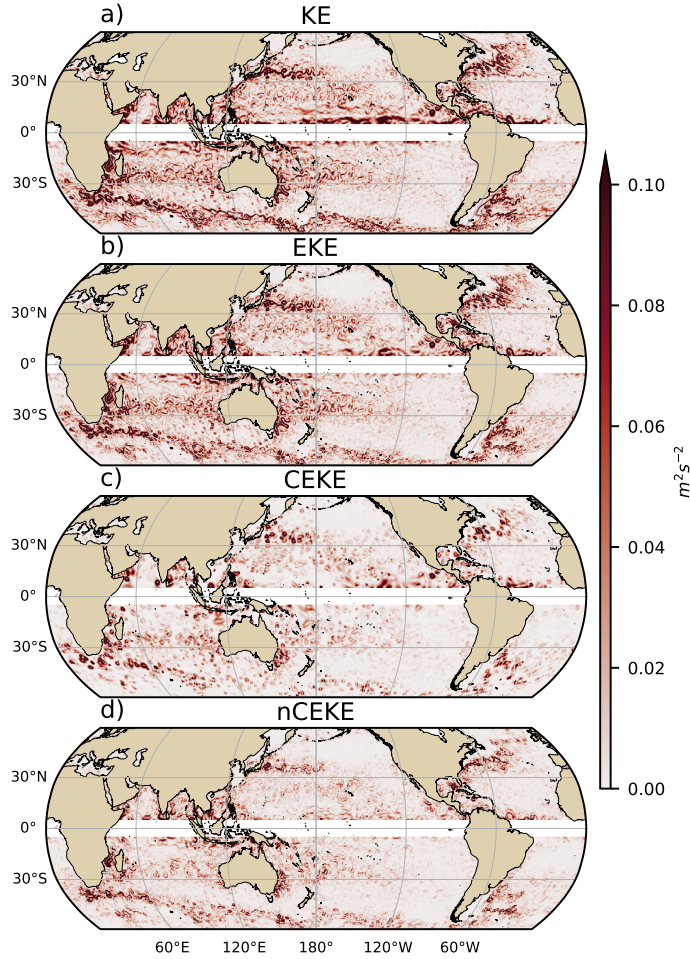
$$\text{KE} = \underbrace{\bar{u}^2 + \bar{v}^2}_{\text{MKE}} + \underbrace{u'^2_e + v'^2_e}_{\text{CEKE}} + \underbrace{u'^2_n + v'^2_n}_{\text{nCEKE}} + \mathcal{O}_c^2 + \mathcal{O}^2 \quad (1)$$

147 Due to the properties of this decomposition, the term \mathcal{O}^2 is zero $\mathcal{O}^2 = \bar{u}u' + \bar{v}v'$
 148 is zero by definition when averaged over the same period as $\bar{\mathbf{u}}$. However, $\mathcal{O}_c^2 = u_e u_n + v_e v_n$
 149 is not necessarily negligible, unless it is averaged over time and space. More information
 150 about the decomposition of the field into coherent features and non-coherent features
 151 is explained in Martínez-Moreno et al. (2019). A global snapshot of each component of
 152 kinetic energy decomposition is shown in Figure 1, where the KE and EKE are comprised
 153 of rings and filaments. As expected, the decomposition of EKE into CEKE and nCEKE
 154 components exhibits only the ring-like signatures expected of coherent eddies, while the
 155 non-coherent component primarily shows filaments, with some mis-identified coherent
 156 eddies.

160 **2.2 Eddy statistics**

161 The eddy statistics used in this study include (i) the eddy count ($cEddy_n$) defined
 162 as the number of coherent eddies per grid cell, (ii) the eddy diameter defined as the di-
 163 ameter of a circle with equal area to the closed contour of each identified eddy, and (iii)
 164 the mean eddy amplitude defined as the mean amplitude of the coherent eddies within
 165 the cell ($cEddy_{amp}$). The latter metric can be separated into positive ($cEddy_{amp}^+$) and
 166 negative ($cEddy_{amp}^-$) coherent eddy amplitudes, defined as the mean amplitude of warm
 167 core and cold core coherent eddies, respectively, within the cell. The polarity indepen-
 168 dent eddy amplitude ($|cEddy_{amp}|$) is defined as:

$$|cEddy_{amp}| = \frac{1}{2} (cEddy_{amp}^+ - cEddy_{amp}^-) \quad (2)$$



157 **Figure 1.** Snapshot of surface kinetic energy (KE), surface eddy kinetic energy (EKE),
 158 surface coherent eddy kinetic energy (CEKE), and surface non-coherent eddy kinetic energy
 159 (nCEKE) for the 1st of January 2017.

169 Note that the $cEddy_{amp}^+$ and $cEddy_{amp}^-$ are sign definite, thus the difference will always
 170 be positive, whereas the gridded averaged $cEddy_{amp}$ can be negative or positive noting
 171 the dominant polarity of coherent eddies in the region, and the absolute value of $cEddy_{amp}$
 172 is denoted by $|cEddy_{amp}|$. We analyze the climatology and trends of the above eddy statis-
 173 tics over the available satellite record, namely between 1993 and 2019. We exclude the
 174 equatorial region ($10^\circ S - 10^\circ N$) and regions poleward of 60° , because the geostrophic ap-
 175 proximation is invalid near the Equator and the satellite spatial coverage at high-latitudes
 176 is unable to resolve the coherent eddy scales polewards of 60° . Note that the climatol-
 177 ogy of $cEddy_n$ is computed by adding all the identified eddies over the record, while all

other climatological statistics are computed as the time-average over the record. Seasonal climatologies are calculated for the monthly average of each coherent eddy statistic, while hemispheric time-series are filtered with a running average of 90 days. Trends of $cEddy_n$ and $|cEddy_{amp}|$ are calculated by coarsening the dataset to a 5° grid, and then linear trends are computed for each grid point. The statistical significance of trends is assessed by a modified Mann-Kendall test above the 95% confidence level (Yue & Wang, 2004).

Time averages are denoted by $\overline{}$, while area-weighted averages are denoted using $\langle \rangle$, where the area-weighted average of a function f is:

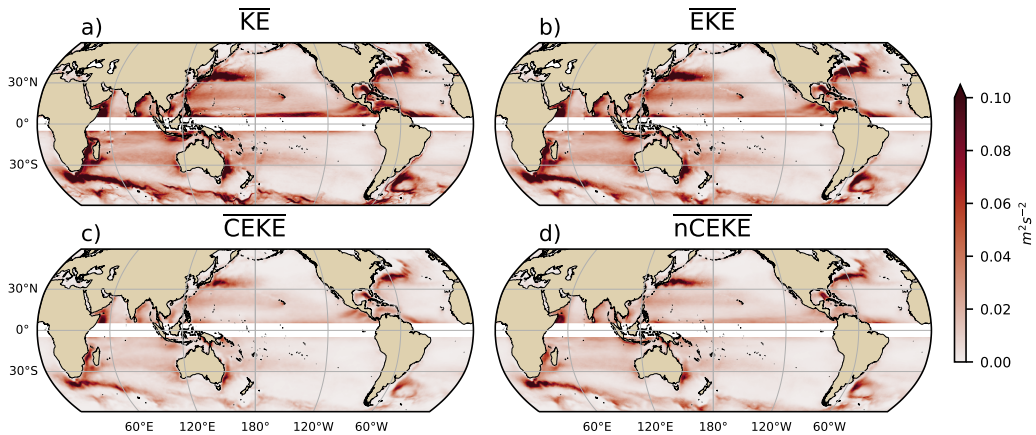
$$\langle f \rangle = \frac{\int f \xi dx dy}{\int \xi dx dy}, \quad (3)$$

where ξ is a mask that is set to zero in grid cells where no coherent eddies were identified and one elsewhere.

3 Global Coherent Eddy Energetics

The kinetic energy decomposition estimated from sea surface height measured by satellite altimeters averaged from 1993-2019 is shown in Figure 2. These maps show that many regions of the global ocean are highly energetic in mean KE (\overline{KE}), mean EKE (\overline{EKE}), mean coherent eddy kinetic energy (\overline{CEKE}) and mean non-coherent eddy kinetic energy (\overline{nCEKE}). The spatial pattern highlights well-known regions of the ocean where mesoscale processes are abundant, such as the western boundary current (WBC) extensions and the Antarctic Circumpolar Current. The spatial distribution of the energy contained by the reconstructed mesoscale coherent eddies and non-coherent components are similar (Figures 2c,d). However, there are some regions where coherent eddies dominate over non-coherent, and vice-versa. Overall, this decomposition suggests that boundary current extensions and other energetic regions of the ocean contain both coherent and non-coherent components of the kinetic energy.

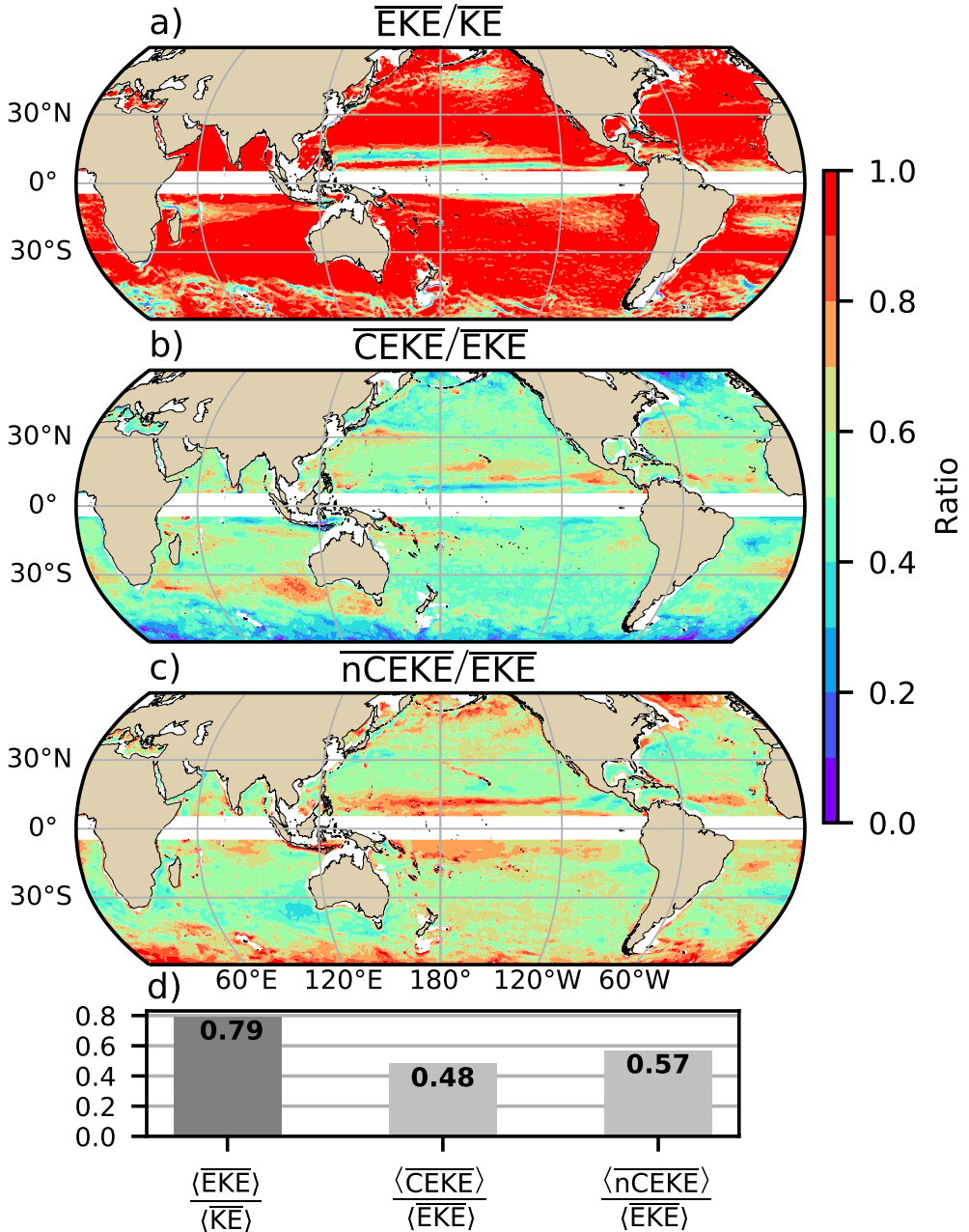
Eddy kinetic energy is known to be more than an order of magnitude greater than kinetic energy of the mean flow (MKE; Gill et al., 1974); this result is clearly shown in Figure 3a, which indicates that \overline{EKE} is responsible for almost all the \overline{KE} across the ocean, except for regions with persistent currents over time. Such regions are located in the mean boundary extension locations, the equatorial Pacific currents and regions in the Antarctic Circumpolar Current, where the \overline{EKE} explains around 40% of the \overline{KE} . In a previ-



202 **Figure 2.** a) Mean surface kinetic energy (\overline{KE}); b) surface eddy kinetic energy (\overline{EKE}); c)
 203 surface coherent eddy kinetic energy (\overline{CEKE}), and d) surface non-coherent eddy kinetic energy
 204 (\overline{nCEKE}) averaged between 1993-2018.

220 ous study, Chelton et al. (2011) estimated that coherent eddies with lifetimes greater than
 221 4 weeks contain between 40-60% of the \overline{EKE} . Our method to reconstruct the coherent
 222 eddy signature (Figure 3b) further corroborates that the coherent eddy component ($\langle \overline{CEKE} \rangle$)
 223 has $\sim 48\%$ of the $\langle \overline{EKE} \rangle$ (Figure 3d). Furthermore, global area averages of the ratios show
 224 that $\langle \overline{EKE} \rangle$ explains $\sim 78\%$ of the ocean $\langle \overline{KE} \rangle$ field, while non coherent eddy features
 225 contain $\sim 57\%$ percent of the $\langle \overline{EKE} \rangle$. Note that the globally averaged coherent and non
 226 coherent components do not add to 100% as the cross terms (O_c^2) are non-zero. The spa-
 227 tial pattern reveals a dominance of the \overline{CEKE} equatorward from the boundary current
 228 extensions and in areas with large coherent eddy contributions of around 80% of the re-
 229 gion's eddy kinetic energy, such as south of Australia, in the Tehuantepec Gulf, and in
 230 the tropical Atlantic. An evident signal is a reduction of the energy contained by coher-
 231 ent eddies at high latitudes and an increase in the energy explained by non-coherent ed-
 232 dies; this signal could be a consequence of the inability of the 0.25° **satellite resolution**
 233 (~ 13 km at 60° latitude) **gridded satellite altimetry** to resolve coherent eddies with scales
 234 smaller than ~ 10 km (first baroclinic Rossby radius at 60° ; Chelton et al., 1998), **as the**
 235 **satellite gridded dataset effective resolution of ~ 25 km at high latitudes and ~ 200 km near**
 236 **the equator (?)**.

237 Figure 4 shows the seasonal cycle of the area-weighted EKE and CEKE for the North-
 238 ern Hemisphere ($\langle EKE \rangle_{NH}$ and $\langle CEKE \rangle_{NH}$; $10^\circ N - 60^\circ N$) and Southern Hemisphere



205 **Figure 3.** Ratios of the kinetic energy components. a) Map of the proportion of mean eddy
 206 kinetic energy ($\overline{\text{EKE}}$) versus mean kinetic energy ($\overline{\text{KE}}$); b) Map of the fraction of mean coherent
 207 eddy kinetic energy ($\overline{\text{CEKE}}$) versus mean eddy kinetic energy ($\overline{\text{EKE}}$); c) Map of the fraction of
 208 mean non-coherent eddy kinetic energy ($\overline{\text{nCEKE}}$) versus mean eddy kinetic energy ($\overline{\text{EKE}}$); d)
 209 Global time and area averaged (represented by $\langle \rangle$) fraction of mean eddy kinetic energy ($\langle \overline{\text{EKE}} \rangle$)
 210 versus the global mean kinetic energy ($\langle \overline{\text{KE}} \rangle$), area averaged fraction of mean coherent eddy
 211 kinetic energy ($\langle \overline{\text{CEKE}} \rangle$) and mean non coherent eddy kinetic energy ($\langle \overline{\text{nCEKE}} \rangle$) versus global
 212 mean eddy kinetic energy ($\langle \overline{\text{EKE}} \rangle$). Regions where the depth of the ocean is shallower than
 213 1000m are removed from the ratio estimation.

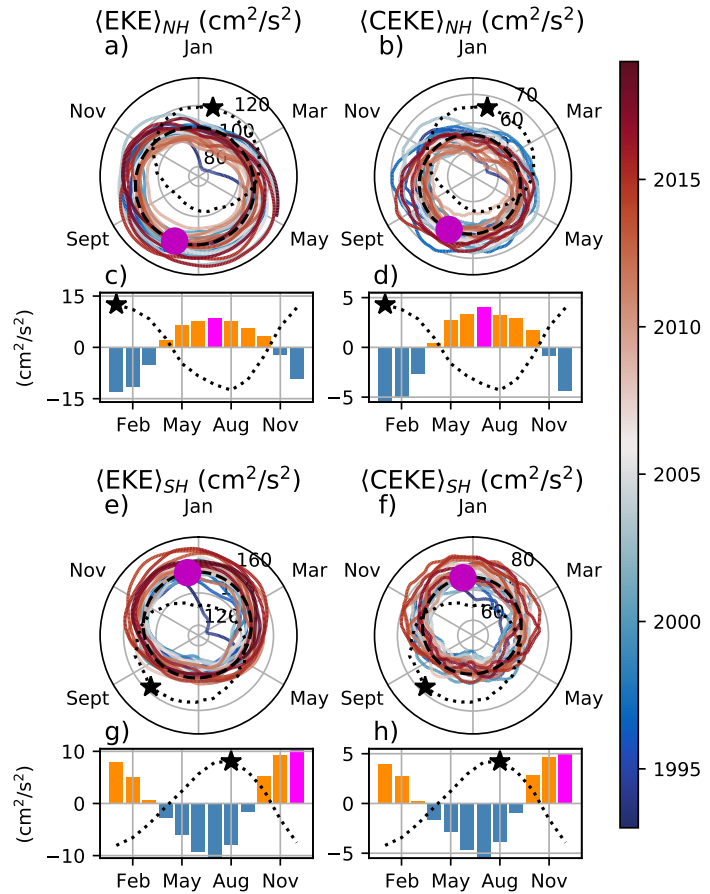
($\langle \text{EKE} \rangle_{SH}$ and $\langle \text{CEKE} \rangle_{SH}$; 60°S - 10°S). In both hemispheres, the $\langle \text{EKE} \rangle$ and $\langle \text{CEKE} \rangle$ peak during summer. In the Northern Hemisphere, the largest $\langle \text{EKE} \rangle_{NH}$ and $\langle \text{CEKE} \rangle_{NH}$ occurs in July, ~6 months after the maximum winds in January (purple bar and black star in Figure 4c and d). Meanwhile, the Southern Ocean $\langle \text{EKE} \rangle_{SH}$ and $\langle \text{CEKE} \rangle_{SH}$ seasonal maxima arise during December, ~4 months after the maximum winds in August (purple bar and back star in Figure 4g, and h). This lag between winds and the eddy and coherent eddy energy components is further discussed in Section 4.

The cyclic plots in Figure 4 show the temporal evolution of $\langle \text{EKE} \rangle$ and $\langle \text{CEKE} \rangle$. Note that high frequency variability can be observed in the $\langle \text{CEKE} \rangle$ field with temporal scales of a few months, this variability could be attributed to regional dynamics averaged over the hemisphere (boundary currents, ocean gyres, etc.), as well as errors within the coherent eddy reconstruction. Additionally, concentric changes in the cyclic plots highlight long-term changes over the record. For example, the Northern Hemisphere winters during early years of the record (blue) had a more energetic coherent eddy field, which has transitioned to weaker coherent energy content since 2010 (red), in other words, the intensity of the $\langle \text{CEKE} \rangle_{NH}$ field has decreased. A larger long-term change can be observed in the Southern Hemisphere, where concentric growth over time in $\langle \text{EKE} \rangle_{SH}$ and $\langle \text{CEKE} \rangle_{SH}$ supports the previously observed strengthening of the eddy field in the Southern Ocean (Hogg et al., 2015; Martínez-Moreno et al., 2019; Martínez-Moreno et al., 2021). Additionally, the seasonal cycle of the $\langle \text{EKE} \rangle$ and $\langle \text{CEKE} \rangle$ peaks during both hemispherical winters, where an increase in SST variance, in conjunction with deeper mixed layers and weaker stratification results in an increase in Baroclinic instability (Callies et al., 2015; Uchida et al., 2017)

261 \wedge

271 4 Global Coherent Eddy Statistics

272 Coherent eddy kinetic energy allows us to quantify and study the energy of the eddy
 273 field, but the coherent eddy properties computed by automated coherent eddy identi-
 274 fication algorithms allow us to further investigate the contribution and temporal changes
 275 of their abundance (i.e. the number of eddies) and their intensity (both their amplitude
 276 and diameter). Figure 5 shows gridded estimates of the number of eddies and the eddy
 277 amplitude. In this analysis, we contrast our MM19 eddy count with that of CS13 (Chel-
 278 ton et al., 2007; Figure 5a-b). Although the number of identified eddies is larger in MM19,
 279 possibly due to the lifespan filter implemented by CS13, both datasets reveal consistent

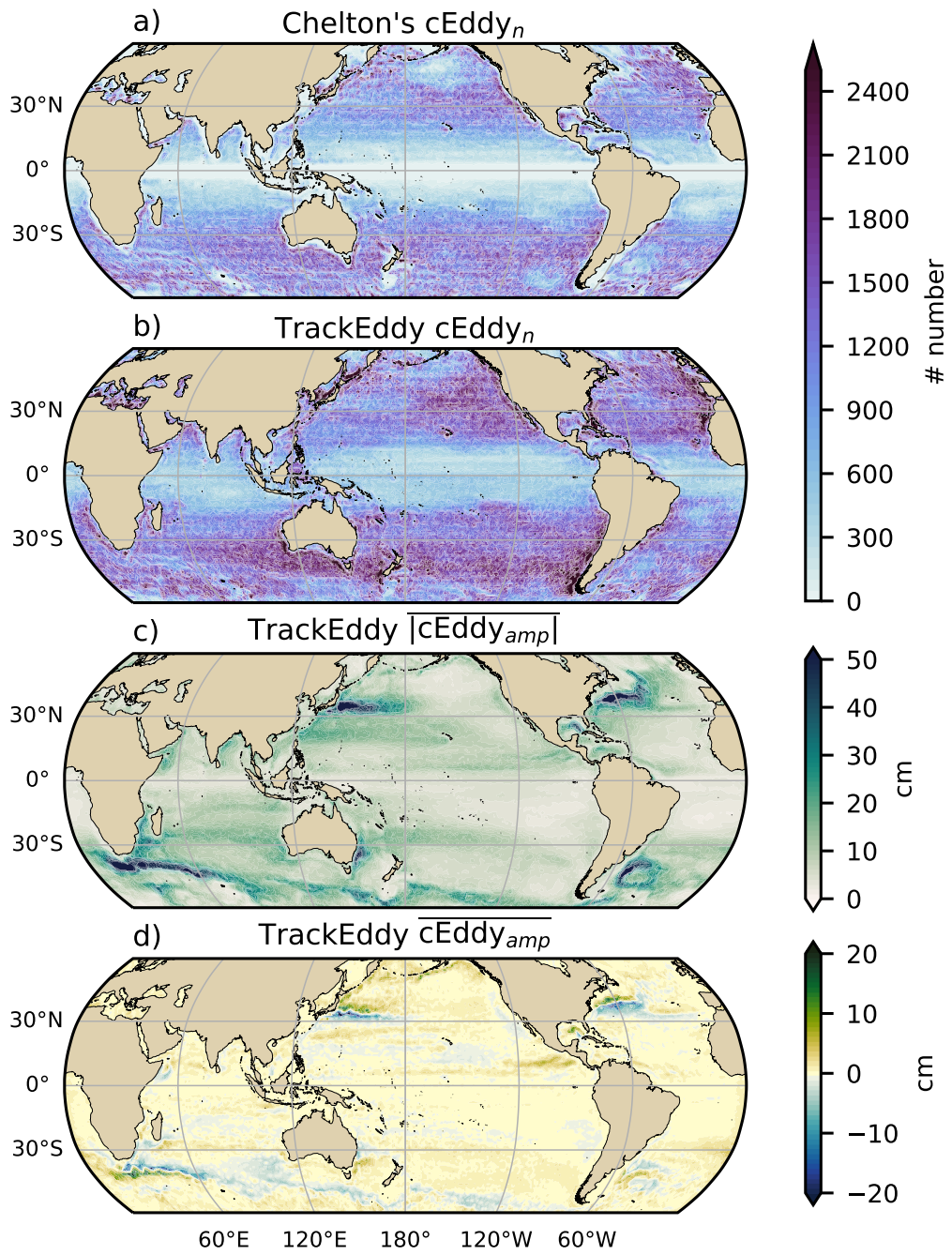


262 **Figure 4.** Seasonality of the area-weighted eddy kinetic energy ($\langle EKE \rangle$) and coherent eddy ki-
 263 netic energy ($\langle CEKE \rangle$). Panels a) and b) show the time-series of the Northern Hemisphere, while
 264 panels e) and f) correspond to the Southern Hemisphere. Panels c) and d) show the seasonal
 265 cycle of the $\langle EKE \rangle_{NH}$ and $\langle CEKE \rangle_{NH}$ in the Northern Hemisphere, and panels g) and h) show
 266 the Southern Hemisphere ($\langle EKE \rangle_{SH}$ and $\langle CEKE \rangle_{SH}$). Bars correspond to the seasonal cycle of
 267 the fields and dotted lines show the seasonal cycle of the wind magnitude smoothed over 120 days
 268 (moving average). The black stars and magenta markers (circle and bar) show the maximum of
 269 the seasonal cycle for the kinetic energy components and the wind magnitude, respectively. In
 270 the cyclic plots, line `colors` shows the year.

280 spatial patterns. For example, both datasets show an important meridional variation in
 281 the abundance of eddies, with high numbers of eddies in mid-latitudes and fewer eddies
 282 in the tropics and at high-latitudes ($\sim 60^\circ$). Additionally, there is a tendency at mid-latitudes
 283 (30°) for higher numbers of eddies in the eastern side of ocean basins (e.g. the East North
 284 Pacific, East North Atlantic, East South Pacific, and East South Atlantic). Another in-
 285 teresting pattern emerges in both eddy count datasets, where small scale structures ap-
 286 pear in the eddy count field. These small structures highlight preferred coherent eddy
 287 paths observable in boundary current extensions and over regions of the Southern Ocean.
 288 These structures and paths of coherent eddies could be associated with topographic fea-
 289 tures, with overall consistency between the eddy count patterns using the two different
 290 eddy identification methods.

296 Regions with large counts of eddies have, in general, small absolute amplitudes (Fig-
 297 ure 5c), for example, the eastern side of mid-latitude ocean basins. The ocean gyre in-
 298 teriors have a larger absolute amplitude and finally regions such as the boundary cur-
 299 rent extensions and the Antarctic Circumpolar Current have the largest coherent eddy
 300 absolute amplitudes, as also shown by Chelton et al. (2011). Eddy amplitude highlights
 301 regions dominated by a given coherent eddy polarity, for example, boundary current ex-
 302 tensions have a preferred sign (Figure 5 d); namely, positive amplitude polewards of the
 303 boundary current extension mean location, and negative amplitude equatorwards. This
 304 sign preference is consistent with the preferential way that coherent eddies are shed from
 305 boundary current extensions; with warm core eddies (positive) polewards of the bound-
 306 ary current extension, and equatorward for cold core eddies (negative) (Chelton et al.,
 307 2007, 2011; Kang & Curchitser, 2013). These global statistics reveal the absolute coher-
 308 ent eddy amplitude as a proxy for the CEKE with similar spatial patterns (Figure 2 &
 309 Figure 5c) and showcases that in regions where $\overline{\text{CEKE}}$ accounts for a large proportion
 310 of $\overline{\text{EKE}}$ (Figure 3), the absolute coherent eddy amplitude is also large.

311 To further understand the seasonal cycle of $\langle \text{CEKE} \rangle$, we compute the climatology
 312 of coherent eddy properties in each hemisphere (Figure 6). The ~~seasonality~~ seasonal maxima
 313 of the number of eddies ~~in occurs in spring; in~~ the Northern Hemisphere ~~peaks in the maxima~~
 314 ~~takes place during~~ April (Figure 6a, c), while the Southern Hemisphere maximum num-
 315 ber of eddies occurs during October (Figure 6e, g). Meanwhile, the ~~seasonality~~ seasonal
 316 maxima of the eddy amplitude ($\langle |c\text{Eddy}_{amp}| \rangle$) ~~arise in winter;~~ peaks in August ~~and January~~
 317 for the Northern ~~and Southern Hemispheres respectively~~ Hemisphere and January in Southern



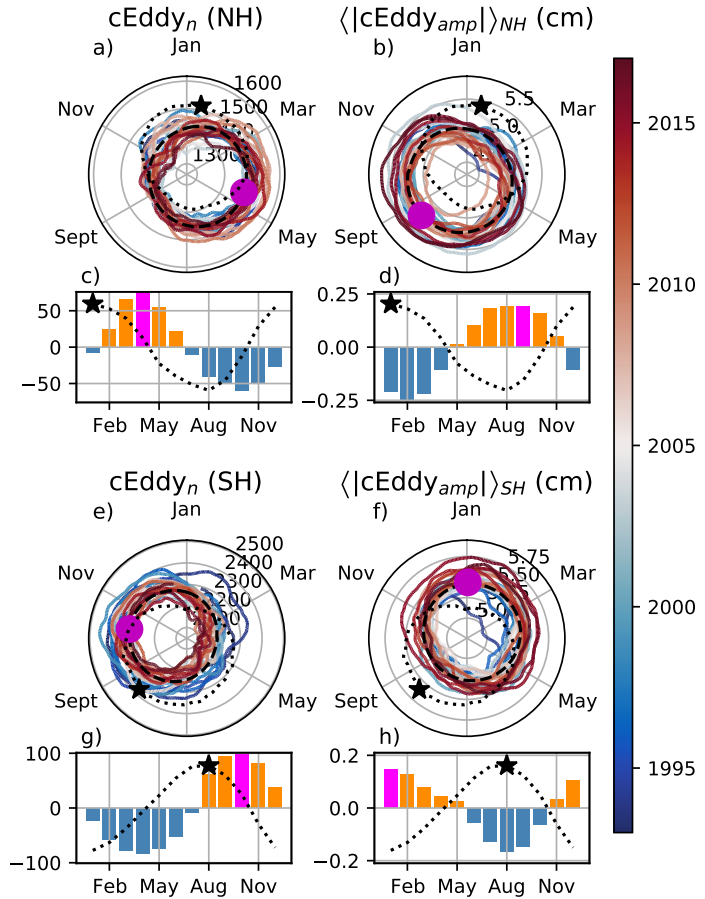
291 **Figure 5.** Averaged coherent eddy statistics. a) Climatology of the number of coherent eddies
 292 (cEddy_n) identified by Chelton et al. (2007); b) Climatology of the number of coherent eddies
 293 (cEddy_n) identified by Martínez-Moreno et al. (2019); c) Climatology of the mean absolute co-
 294 herent eddy amplitude (cEddy_{amp}), and d) Climatology of the mean coherent eddy amplitude
 295 (cEddy_{amp}).

³¹⁸ Hemisphere (Figure 6b, d, f, and h). As expected, the seasonality of $\langle |cEddy_{amp}| \rangle$, equivalent
³¹⁹ to the intensity of the coherent eddies, ~~is consistent~~ coincides with the seasonal cycle of $\langle CEKE \rangle$.
³²⁰

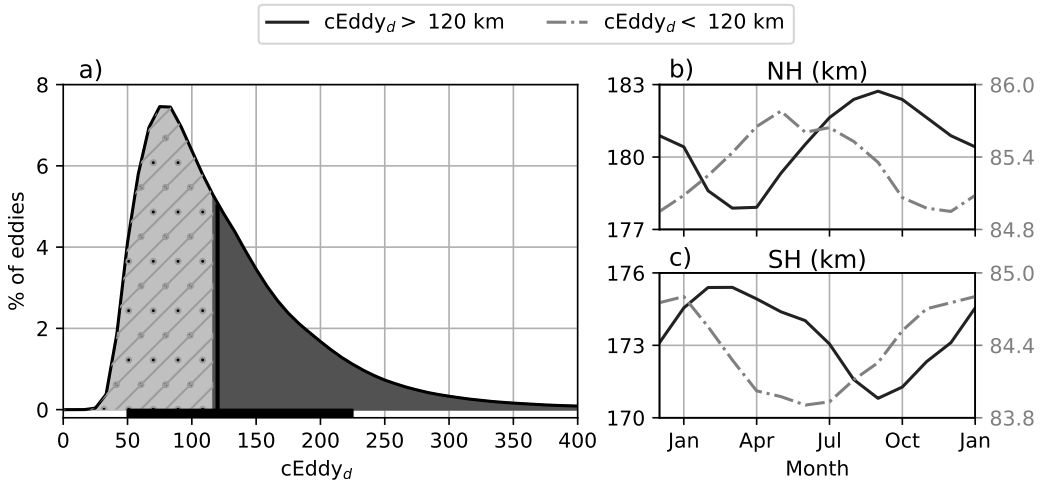
³²¹ A key feature of Figure 6 is a distinct lag of ~ 3 months between the winds and eddy
³²² count, while the eddy amplitude maximum occurs ~ 6 months after the seasonal max-
³²³ imum in winds. We suggest that the eddy number increases earlier in the year and, through
³²⁴ eddy-eddy interactions (for example, merging of coherent eddies), the coherent eddy am-
³²⁵ plitude increases ~ 3 months after. This seasonal lag and summer maximum is consis-
³²⁶ tent with previous studies which suggest that a time-lag of the inverse cascade (Sasaki
³²⁷ et al., 2014; Qiu et al., 2014) is responsible for the EKE seasonal cycle, where winter has
³²⁸ the highest energy at the smallest scales (non-resolvable with satellite observations), spring
³²⁹ and autumn have the highest and lowest energy at scales of 50-100 km, and summertime
³³⁰ has the highest energy at the largest scales (> 100 km; Uchida et al., 2017). Thus, the
³³¹ maximum of $\langle EKE \rangle$, $\langle CEKE \rangle$, and $\langle |cEddy_{amp}| \rangle$ located during summertime suggests
³³² that the seasonality of eddies and coherent eddies could be dominated by scales larger
³³³ than 100 km.

³³⁴ This result can be further explored by looking at the seasonal evolution of the eddy
³³⁵ diameter ($cEddy_d$). Note that 90% of identified coherent eddies have diameters between
³³⁶ 50 and 220 km (Figure 7a). We partition eddies into large-scale coherent eddies (diam-
³³⁷ eter > 120 km) and small-scale coherent eddies (diameter < 120 km; Figure 7a). In the
³³⁸ Northern Hemisphere, small-scale eddies have a seasonal peak in diameter during May,
³³⁹ while large-scale eddies have the greatest diameter in September (Figure 7b). Meanwhile,
³⁴⁰ in the Southern Hemisphere, the small-scale coherent eddies exhibit maximum diame-
³⁴¹ ter in December, while the diameter of large-scale coherent eddies peaks in February (Fig-
³⁴² ure 7 c). This result suggests that wind driven baroclinic instabilities generate small co-
³⁴³ herent eddies early in the season, which then merge and grow to become larger in diam-
³⁴⁴ eter and amplitude, and thus, more energetic. This process is likely associated with the
³⁴⁵ inverse energy cascade, and suggests that this mechanism not only drives EKE season-
³⁴⁶ ality, but also may be responsible for the seasonal cycle of coherent eddies.

³⁶³ Long-term changes can be observed in Figure 6a,b, e, and f where growing/shrink-
³⁶⁴ ing concentric circles over time denote an trend of the field. This trend is particularly
³⁶⁵ evident in the Southern Hemisphere, where the number of eddies has decreased, while



347 **Figure 6.** Seasonality of the count of number of eddies ($c\text{Eddy}_n$) and the area-weighted polar-
 348 349 350 351 352 353 354 355 ity independent coherent eddy amplitude ($\langle |c\text{Eddy}_{amp}| \rangle$); Panels a and b show the time-series of
 the Northern Hemisphere, while panels e and f correspond to the Southern Hemisphere. Panels c
 and d show the seasonal cycle of $c\text{Eddy}_n$ and $\langle |c\text{Eddy}|_{amp} \rangle_{NH}$ in the Northern Hemisphere, and
 panels g and h show the Southern Hemisphere, $c\text{Eddy}_n$ and $\langle |c\text{Eddy}|_{amp} \rangle_{SH}$. Bars correspond to
 the seasonal cycle of the fields and dotted lines show the seasonal cycle of the wind magnitude,
 smoothed over 120 days (moving average). The black stars and magenta markers (circle and
 bar) indicate the maximum of the seasonal cycle for the eddy property, and the wind magnitude,
 respectively. In the cyclic plots, line color show the year from 1993-2019.



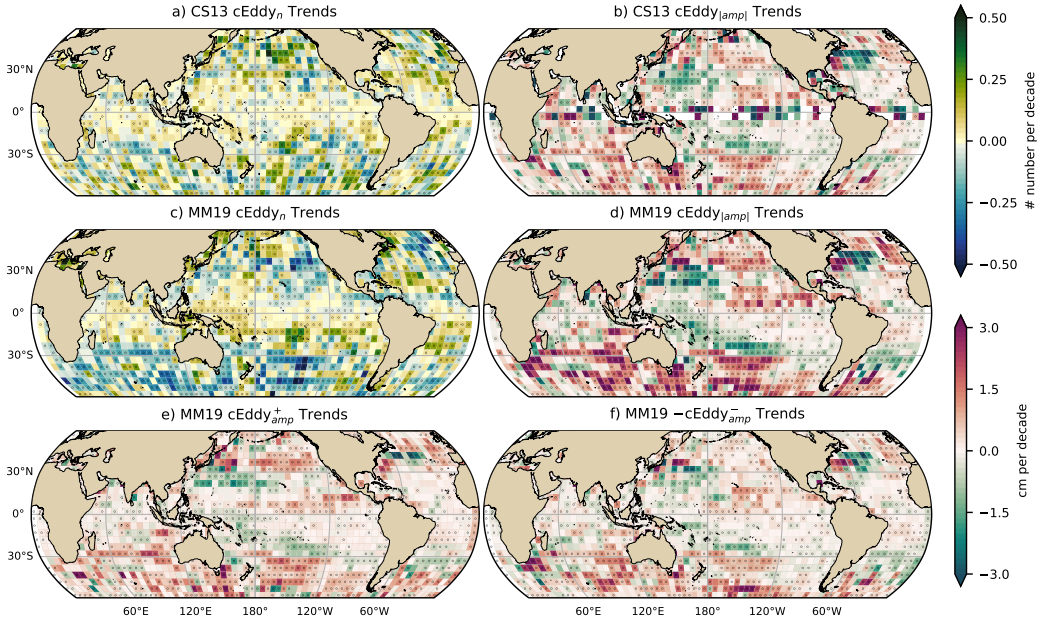
356 **Figure 7.** Distribution of the identified eddy diameter ($cEddy_d$; km) and hemispherical
 357 seasonality of the coherent eddy diameter. a) Distribution in percentage of identified eddy am-
 358 plitude, solid bar below distribution represents 90% of the identified eddies. Seasonal cycle of the
 359 eddy diameter for the b) Northern Hemisphere and c) Southern Hemisphere. Dark solid line and
 360 area corresponds to coherent eddies with diameters larger than 120 km, while light gray dash-
 361 dotted line and area shows coherent eddies with diameters smaller than 120 km. [Gray envelopes in](#)
 362 [b\) and c\) show seasonal changes in 100 randomly sub-sample 1% of the data \(\$n \sim 345000\$ \).](#)

366 the eddy amplitude has increased. This result is consistent with the observed trends in
 367 EKE and mesoscale EKE in the Southern Ocean (Hogg et al., 2015; Martínez-Moreno
 368 et al., 2019). The coherent eddy amplitude from positive coherent eddies and negative
 369 coherent eddies show similar seasonal cycles to the absolute eddy amplitude. The North-
 370 ern Hemisphere decrease in absolute eddy amplitude is driven by a decrease of the am-
 371 plitude of negative coherent eddies in the Northern Hemisphere. Meanwhile in the South-
 372 ern Ocean, the increase in absolute eddy amplitude is corroborated by a strengthening
 373 of both coherent eddy polarities since the early 90s.

374 5 Trends

375 The results presented in Figures 4 and 6 suggest a long-term readjustment of the
 376 coherent eddy field. The long-term trends of the number of coherent eddies, absolute co-
 377 herent eddy amplitude, and coherent eddy amplitude polarities are further explored in
 378 Figure 8 contrasting the MM19 and CS13 methods. Both MM19 and CS13 datasets show
 379 consistent spatial patterns in the trends and significance of the number of coherent ed-
 380 dies and the absolute coherent eddy amplitude. Several regions in the ocean, such as the
 381 Southern Ocean, North Atlantic and North Pacific, show a decrease in the number of ed-
 382 dies. Those same regions also have a clear increase in the absolute coherent eddy am-
 383 plitude. These trends are similar to those observed in mesoscale eddy kinetic energy (Martínez-
 384 Moreno et al., 2021) and provide additional evidence of a readjustment of the mesoscale
 385 eddy field over the last 3 decades.

386 The observed trends of $cEddy_{amp}$ in several oceanic regions have the same scale
 387 as sea level rise ($\sim 3\text{cm}$ per decade). By analyzing the positive and negative coherent eddy
 388 amplitude, we filter out the observed trends that come from a net increase in sea level.
 389 In fact, each coherent eddy polarity has intensified in the Southern Ocean and North East
 390 Pacific and Atlantic. In other words, the amplitude of each polarity has increased over
 391 time, and thus this strengthening is an intrinsic response of the coherent eddy field. Note
 392 that the negative coherent eddy amplitude dominates the global $|cEddy_{amp}|$ trends (Fig-
 393 ure 8e, f). However, different trend patterns can be observed in both positive and neg-
 394 ative coherent eddy amplitudes in the North Atlantic and North Pacific, where the neg-
 395 ative coherent eddy amplitude in the Western Boundary Currents appears to decrease.



396 **Figure 8.** Trends of coherent eddy statistics. a) and c) Trends of the number of identified
 397 coherent eddies from satellite observations identified reported in CS13's dataset and using the
 398 TrackEddy scheme of MM19. b) and d) Trends of the absolute value of identified coherent eddy
 399 amplitude ($cEddy_{|amp|}$) from satellite observations reported by CS13 and TrackEddy (after
 400 MM19). e) and f) Trends of the eddy amplitude polarity using TrackEddy ($cEddy_{amp}^+$ and
 401 $cEddy_{amp}^-$). Gray stippling shows regions that are statistically significant above the 95% con-
 402 fidence level.

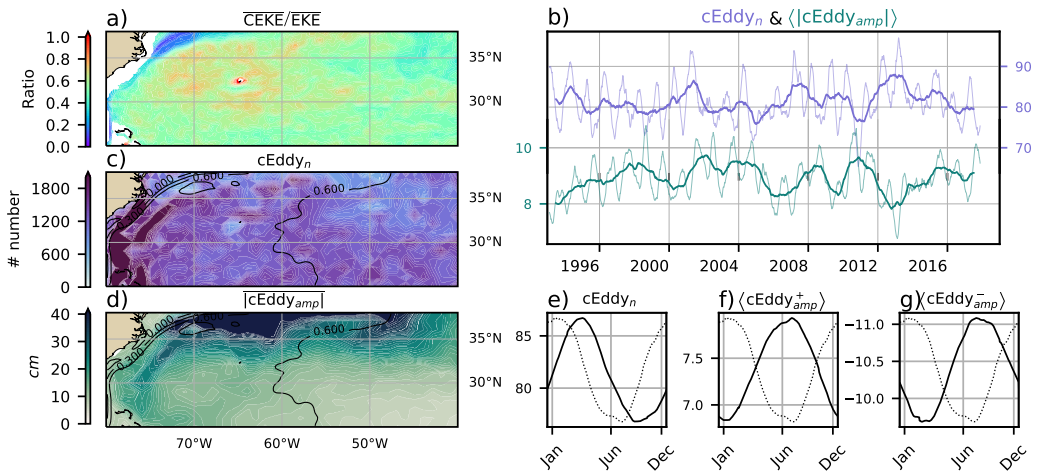
403 **6 Regional Climatology**

404 For regions with relatively large proportions of CEKE located at WBC extensions
 405 and eastern boundary currents, we investigate the seasonal and long-term variability of
 406 the coherent eddy properties. The most energetic WBCs include the Gulf Stream, the
 407 Kuroshio Current, and the Agulhas Current (Figures 9, 10, and 11). Coherent eddy gen-
 408 eration in boundary current extensions occurs through baroclinic and barotropic insta-
 409 bilities of the mean current, thus all these regions share similar generation dynamics. In
 410 all these regions without exception; (i) CEKE contains 50-80% of the EKE in regions
 411 equatorward from the mean WBC extensions, (ii) the number of eddies is consistently
 412 small over the mean WBC extensions, and (iii) the eddy amplitude is larger over the mean
 413 WBC extensions.

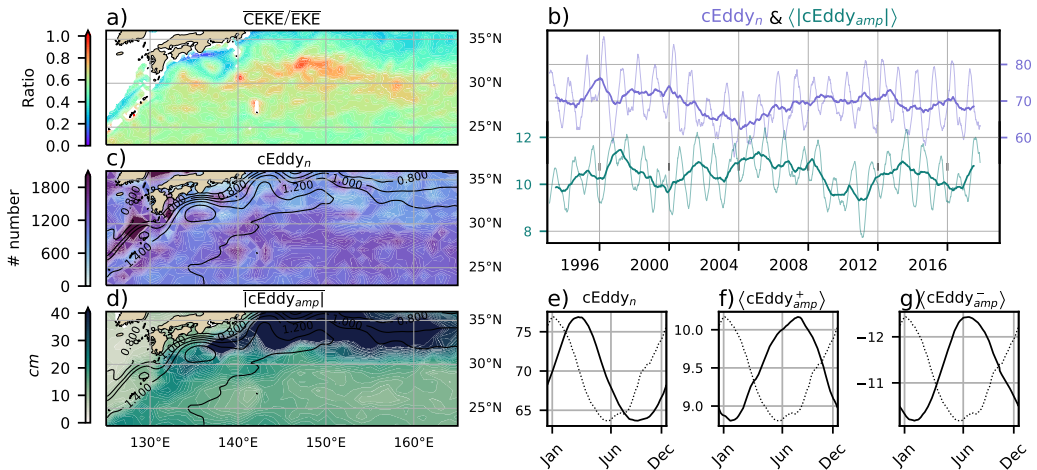
414 In the Gulf Stream, the energy ratio between CEKE and EKE is \sim 56% (Figure 9).
 415 The highest energy ratio occurs in regions with numerous eddies, colocated with regions
 416 where the largest $|cEddy_{amp}|$ gradients occur. The time series of $cEddy_n$ and $\langle |cEddy_{amp}| \rangle$
 417 are anti-correlated (-0.52), and they display interannual and seasonal variability. Although
 418 Chaudhuri et al. (2009) observed that a positive phase of the North Atlantic Oscillation
 419 (NAO) exhibits higher EKE, due to an increase in baroclinic instability, thus suggest-
 420 ing more coherent eddies, we do not find a correlation between the $cEddy_n$ or the $\langle |cEddy_{amp}| \rangle$
 421 in the Gulf Stream and the NAO index. Similar to the signal observed in the hemispheric
 422 analysis, the eddy count seasonal cycle follows the wind maximum lagging by \sim 3 months,
 423 while the amplitude of the coherent eddies lags by \sim 6 months.

433 The variability of the $cEddy_n$ and $\langle |cEddy_{amp}| \rangle$ in the Kuroshio Current are weakly
 434 anti-correlated (-0.41; Figure 10). However, on average 56% of the energy in the region
 435 corresponds to CEKE. As observed in the Gulf Stream, there is an important seasonal
 436 cycle in the boundary current extension, where the eddy count seasonal cycle peak oc-
 437 curs in March, lagging the wind maximum by \sim 3 months (January). Meanwhile, the am-
 438 plitude of the coherent eddies lags the wind maximum by \sim 6 months (June).

445 In the Southern Hemisphere the strongest boundary current, the Agulhas Current,
 446 shows similar behavior to its counterparts in the Northern Hemisphere (Figure 11). On
 447 average, coherent eddies in the Agulhas Current contain \sim 56% of the energy, meanwhile
 448 the $cEddy_n$ seasonal peak occurs in August, while the $\langle |cEddy_{amp}| \rangle$ peak occurs in January-
 449 February. The seasonal lag between the winds, eddy count, and eddy amplitude in each



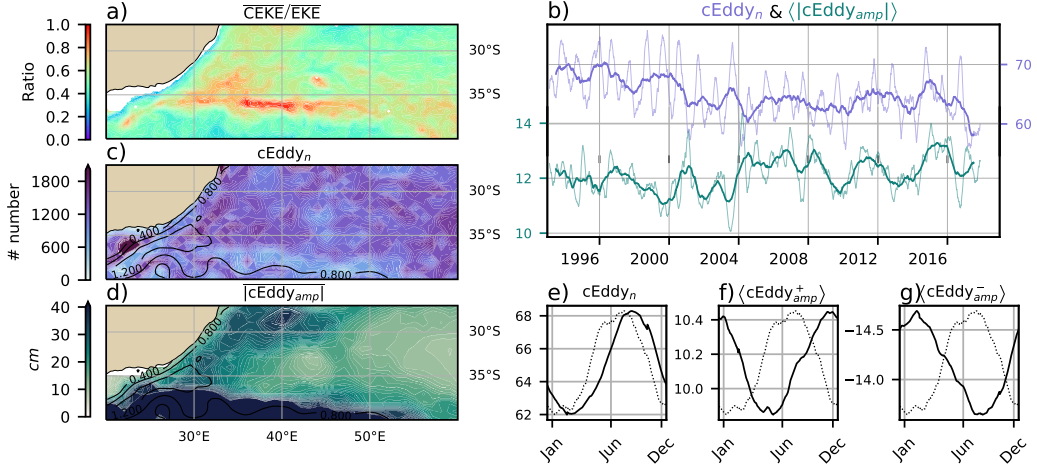
424 **Figure 9.** Climatology of the eddy field and coherent eddy field in the Gulf Stream. a) Ratio
 425 of mean coherent eddy kinetic energy ($\overline{\text{CEKE}}$) versus mean eddy kinetic energy ($\overline{\text{EKE}}$); b) Thick
 426 lines show the running average over 2 years and thin lines show the running average over 90 days
 427 of the coherent eddy number sum and the average coherent eddy amplitude; c) Map of the num-
 428 ber of eddies; d) Map of the average coherent eddy amplitude; e) Seasonal cycle of the number
 429 of eddies ($c\text{Eddy}_n$); f) Seasonal cycle of the positive coherent eddy amplitude ($\langle c\text{Eddy}_{amp}^+ \rangle$),
 430 and g) Seasonal cycle of the negative coherent eddy amplitude ($\langle c\text{Eddy}_{amp}^- \rangle$). Contours in maps
 431 correspond to mean sea surface height (m). Dotted lines show the seasonal cycle of the wind
 432 magnitude.



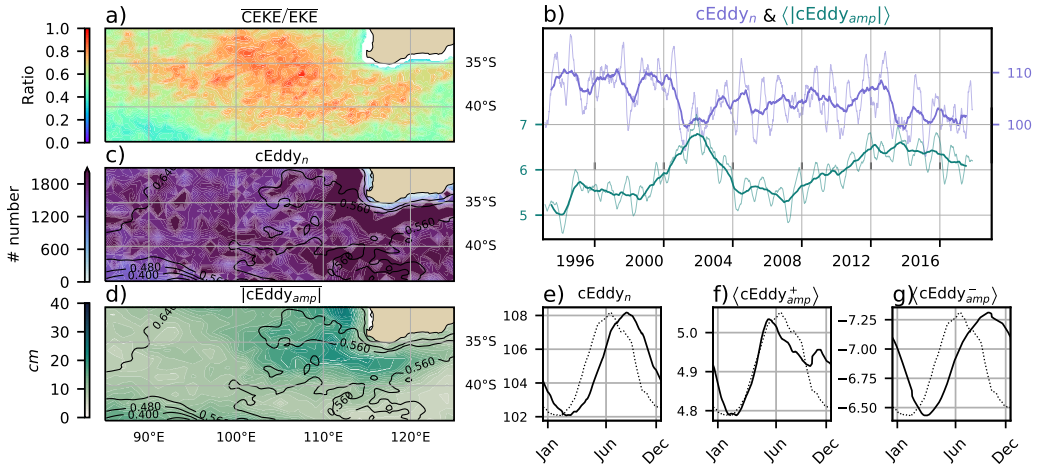
439 **Figure 10.** As in Figure 9, only showing the climatology of the eddy field and coherent eddy
 440 field in the Kuroshio extension. a) Ratio of mean coherent eddy kinetic energy (\overline{CEKE}) versus
 441 mean eddy kinetic energy (\overline{EKE}); b) Time-series of the coherent eddy number and the average
 442 coherent eddy amplitude; c) Map of the number of eddies; d) Map of the average coherent eddy
 443 amplitude; Seasonal cycle of the e) number of eddies; f) positive coherent eddy amplitude, and g)
 444 negative coherent eddy amplitude.

450 of the WBC extensions is interpreted as being analogous to the lagged response of co-
 451 herent eddy properties (Figure 6) due to eddy-eddy interactions, consistent with the in-
 452 verse cascade of energy.

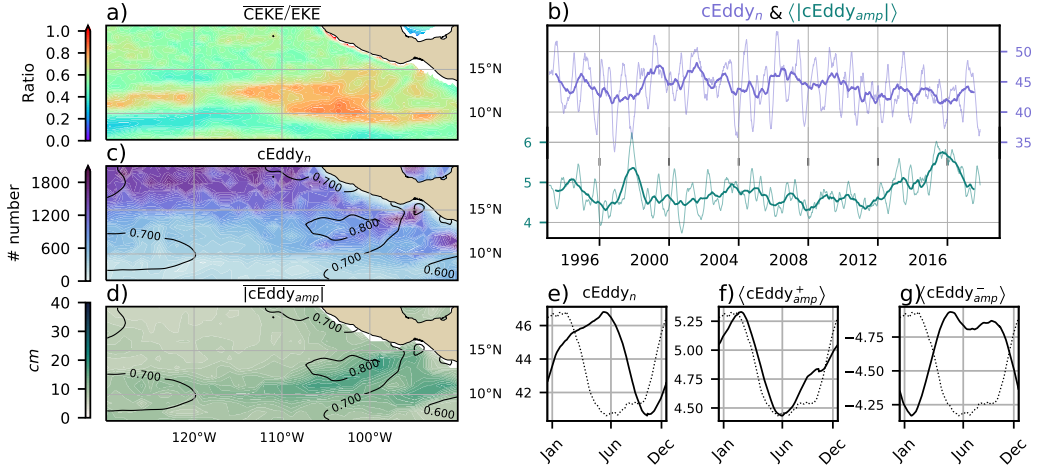
459 Coherent eddies dominate the EKE field in other regions such as the Leeuwin Cur-
 460 rent (Figure 12), where 65% of the energy is contained in coherent eddies. The Leeuwin
 461 region is not characterized by having a large EKE, however, a considerable abundance
 462 of eddies and large eddy amplitudes are observed in the region. The time-series reveal
 463 a significant increase in the $\langle |cEddy_{amp}| \rangle$, while the $cEddy_n$ has decreased over the last
 464 3 decades. The seasonal cycle shows that the $cEddy_n$ peak occurs in August, 3 months
 465 after the maximum winds (June). Meanwhile, the $\langle cEddy_{amp}^+ \rangle$ responds in synchrony
 466 to the winds, and the $\langle cEddy_{amp}^- \rangle$ is in phase with the seasonal cycle of the eddy num-
 467 ber ($cEddy_n$). Hence, this region contrasts with the behavior of WBC extensions, and
 468 showcases the spatial variability of the seasonal cycle of coherent eddies.



453 **Figure 11.** As in Figure 9, only showing the climatology of the eddy field and coherent eddy
 454 field in the Agulhas Current. a) Ratio of mean coherent eddy kinetic energy ($\overline{\text{CEKE}}$) versus
 455 mean eddy kinetic energy ($\overline{\text{EKE}}$); b) Time-series of the coherent eddy number and the average
 456 coherent eddy amplitude; c) Map of the number of eddies; d) Map of the average coherent eddy
 457 amplitude; Seasonal cycle of the e) number of eddies; f) positive coherent eddy amplitude, and g)
 458 negative coherent eddy amplitude.



469 **Figure 12.** As in Figure 9, only showing the climatology of the eddy field and coherent eddy
 470 field in the Leeuwin Current. a) Ratio of mean coherent eddy kinetic energy ($\overline{\text{CEKE}}$) versus
 471 mean eddy kinetic energy ($\overline{\text{EKE}}$); b) Time-series of the coherent eddy number and the average
 472 coherent eddy amplitude; c) Map of the number of eddies; d) Map of the average coherent eddy
 473 amplitude; Seasonal cycle of the e) number of eddies; f) positive coherent eddy amplitude, and g)
 474 negative coherent eddy amplitude.



488 **Figure 13.** As in Figure 9, only showing the climatology of the eddy field and coherent eddy
 489 field in the East Tropical Pacific. a) Ratio of mean coherent eddy kinetic energy ($\overline{\text{CEKE}}$) versus
 490 mean eddy kinetic energy ($\overline{\text{EKE}}$); b) Time-series of the coherent eddy number and the average
 491 coherent eddy amplitude; c) Map of the number of eddies; d) Map of the average coherent eddy
 492 amplitude; Seasonal cycle of the e) number of eddies; f) positive coherent eddy amplitude, and g)
 493 negative coherent eddy amplitude.

475 Another region with important contributions to the coherent eddy field is the East
 476 Tropical Pacific (Tehuantepec region; Figure 13), where coherent eddies contain $\sim 58\%$
 477 of the energy. In fact, coherent eddy generation in this region is modulated by winds and
 478 coastally trapped waves which produce a strong horizontal and vertical shear (baroclinic
 479 and barotropic instabilities; Zamudio et al., 2006). Furthermore, the equatorial gener-
 480 ated waves propagating along the coast have an important interannual variability ob-
 481 servable in the $\langle |c\text{Eddy}_{amp}| \rangle$ time-series, where El Niño events are notable during 1997
 482 and 2015 (Figure 13b). The seasonal cycle of $c\text{Eddy}_n$, $\langle c\text{Eddy}_{amp}^+ \rangle$, and $\langle c\text{Eddy}_{amp}^- \rangle$ sup-
 483 port the idea of a coherent eddy response to two different coherent eddy generation mech-
 484 anisms; the number of eddies lags by ~ 3 months from the winds, while the $\langle c\text{Eddy}_{amp}^+ \rangle$
 485 is in phase with the winds and the time of maximum trapped wave activity (winter; Za-
 486 mudio et al., 2006), while the $\langle c\text{Eddy}_{amp}^- \rangle$ could be a consequence of eddy-eddy inter-
 487 actions.

494 **7 Discussion and Conclusions**

495 We have investigated the contribution of coherent eddies to the total kinetic en-
 496 ergy field using available satellite observations. We found that around half of the EKE
 497 is explained by coherent eddies. This half is concentrated in eddy-rich regions where a
 498 recent multi-decadal intensification of the eddy field has been observed (Martínez-Moreno
 499 et al., 2021). The energy contained by eddies is larger than the previous estimate of 40%
 500 by Chelton et al. (2011). Although there are differences in the identification criteria of
 501 both eddy identification methods, the main cause of the difference is likely to be the life-
 502 span and amplitude filters. These filters are widely used to track individual eddies in space
 503 and time, however, interactions between eddies in energetic regions may obscure the abun-
 504 dance and influence of short-lived coherent eddies. Filters are not used in this study, and
 505 indeed a lack of filters could facilitate an over-estimation of the the energy contained by
 506 coherent eddies, when mis-identifying or mis-fitting a coherent eddy.

507 It should also be noted that regions with first baroclinic Rossby radius of defor-
 508 mation smaller than ~~10km~~-25km cannot be resolved by satellite observations. Thus, the
 509 energy contained in coherent eddies around latitudes of 60° and those near the shore are
 510 missed from this estimate, and their role in the seasonal cycle and local dynamics remains
 511 unknown. New satellite altimeter missions (e.g. Surface Water and Ocean Topography;
 512 SWOT) may allow estimates of the energy contained in mesoscale coherent eddies out-
 513 side the subtropical regions and over the continental slope.

514 Hemisphere-wide variability indicates a strong seasonal cycle of the EKE, CEKE,
 515 and eddy properties. The seasonal cycle of the CEKE in each hemisphere occurs as a
 516 consequence of numerous small coherent eddies interacting with each other (eddy-eddy
 517 interactions) and resulting in stronger, larger and more energetic (but fewer) coherent
 518 eddies during summer, a few months after the yearly coherent eddy number maximum.
 519 This result reveals eddy-eddy interactions and thus the transfer of energy from smaller
 520 coherent eddies to larger coherent eddies could explain the observed seasonal cycle of CEKE
 521 and coherent eddies properties.

522 Coherent eddy properties reveal a non-uniform long-term readjustment of the mesoscale
 523 eddy field. Overall, the eddy number has decreased globally at a significant rate of ∼35
 524 eddies per decade from ∼4000 eddies identified globally on average each day. Despite the
 525 small changes in the total eddy numbers, large proportions of the ocean show a major

strengthening of the mesoscale coherent eddy amplitude at rates greater than ~ 1 cm per decade. This strengthening of the coherent eddy amplitude is attributed to an intensification of each coherent eddy polarity, rather than a readjustment of the coherent eddy field to sea level rise. In other words, the coherent eddy amplitude intensification is occurring in both coherent eddy polarities and a proportion of the previously observed readjustments in the eddy field to long-term changes in the ocean forcing (Hu et al., 2020; Wunsch, 2020; Martínez-Moreno et al., 2021). This long-term readjustment reveals an intensification of the coherent eddy field, possibly due to long-term readjustments in the ocean baroclinic and barotropic instabilities, as well as the strength of the winds.

The reconstruction of the coherent eddies and their statistics has revealed regions with important coherent eddy contributions and a distinct seasonal evolution of the coherent eddies. Western boundary current (WBC) extensions generate eddies through the instability of the main currents and the seasonal cycle of coherent eddies, CEKE, and thus EKE could be associated with an inverse energy cascade observable through lagged seasonal cycles in the coherent eddy statistics. In addition, the amplitude of the seasonal cycle in WBC extensions is two times larger than any other region, thus the seasonality of the coherent eddies in WBC extensions dominates the hemispheric seasonal cycle. Furthermore, the seasonal lag of the inverse energy cascade is coupled with the presence of fronts (Qiu et al., 2014), such as the case for WBC extensions, and our results are consistent with the notion of baroclinic instability generating eddies and, via eddy-eddy interactions, a lagged inverse energy cascade.

The use of satellite observations in this study limits our ability to quantify the importance of the inverse energy cascade seasonality in the control of the coherent eddy seasonal cycle. As mentioned above, there is robust evidence of an increase in eddy-eddy interactions, however we cannot discard important contributions from other processes such as the seasonal cycle of forcing, stratification, and instabilities, which are crucial in the generation of coherent eddies. Although this study can provide a descriptive response of the coherent eddy field, further work is needed to assess the role of eddy-eddy interactions in our changing climate, ocean dynamics, and biogeochemical processes. Furthermore, the SWOT mission could allow us to advance our understanding of eddy-eddy interactions and the seasonal cycle of scales smaller than mesoscale, which may provide further evidence of the inverse energy cascade driving the coherent eddy seasonality. Current generation climate models have just started to resolve mesoscale dynamics, thus,

559 the presented estimate of energy in coherent eddies from satellite observations could be
 560 used as a benchmark that facilitates the evaluation of such models, and to quantify the
 561 energy contained by mesoscale and more specifically coherent eddies in future climate
 562 projections.

563 **Acknowledgments**

564 The Chelton & Schlaak (2013) dataset was produced by SSALTO/DUACS and distributed
 565 by AVISO+ (<https://www.aviso.altimetry.fr/>) with support from CNES, developed
 566 and validated in collaboration with E.Mason at IMEDEA. Global coherent eddy recon-
 567 struction, coherent and non-coherent eddy kinetic energy datasets, in addition to grid-
 568 ded coherent eddy tracking datasets are publicly available at (<https://doi.org/10.5281/zenodo.4646429>). All analyses and figures in this manuscript are reproducible via Jupyter
 569 notebooks and instructions can be found in the Github repository `CEKE_climatology`
 570 (https://github.com/josuemtzmo/CEKE_climatology). Trends used the Python Pack-
 571 age `xarrayMannKendall` (<https://doi.org/10.5281/zenodo.4458776>). J.M.-M. was
 572 supported by the Consejo Nacional de Ciencia y Tecnología (CONACYT), Mexico fund-
 573 ing. M.H.E. is supported by the Centre for Southern Hemisphere Oceans Research (CSHOR),
 574 a joint research centre between Qingdao National Laboratory for Marine Science and Tech-
 575 nology (QNLM), Commonwealth Scientific and Industrial Research Organisation (CSIRO),
 576 University of New South Wales (UNSW), and the University of Tasmania (UTAS). Anal-
 577 yses were undertaken on the National Computational Infrastructure in Canberra, Aus-
 578 tralia, which is supported by the Australian Commonwealth Government.
 579

580 **References**

- 581 Arbic, B. K., Polzin, K. L., Scott, R. B., Richman, J. G., & Shriver, J. F. (2013).
 582 On Eddy Viscosity, Energy Cascades, and the Horizontal Resolution of Gridded
 583 Satellite Altimeter Products*. *Journal of Physical Oceanography*, 43(2), 283–300.
 584 doi: 10.1175/jpo-d-11-0240.1
- 585 Ashkezari, M. D., Hill, C. N., Follett, C. N., Forget, G., & Follows, M. J. (2016).
 586 Oceanic eddy detection and lifetime forecast using machine learning methods.
 587 *Geophysical Research Letters*, 43(23). doi: 10.1002/2016gl071269
- 588 Beron-Vera, F. J., Wang, Y., Olascoaga, M. J., Goni, G. J., & Haller, G. (2013). Ob-
 589 jective Detection of Oceanic Eddies and the Agulhas Leakage. *Journal of Physical*

- 590 *Oceanography*, 43(7), 1426–1438. doi: 10.1175/JPO-D-12-0171.1
- 591 Bouali, M., Sato, O. T., & Polito, P. S. (2017). Temporal trends in sea surface tem-
592 perature gradients in the South Atlantic Ocean. *Remote Sensing of Environment*,
593 194, 100–114. doi: 10.1016/j.rse.2017.03.008
- 594 Callies, J., Flierl, G., Ferrari, R., & Fox-Kemper, B. (2015). The role of mixed-layer
595 instabilities in submesoscale turbulence. *Journal of Fluid Mechanics*, 788, 5–41.
596 doi: 10.1017/jfm.2015.700
- 597 Cane, M. A., Clement, A. C., Kaplan, A., Kushnir, Y., Pozdnyakov, D., Seager, R.,
598 ... Murtugudde, R. (1997). Twentieth-Century Sea Surface Temperature Trends.
599 *Science*, 275(5302), 957–960. doi: 10.1126/science.275.5302.957
- 600 Chaudhuri, A. H., Gangopadhyay, A., & Bisagni, J. J. (2009). Interannual variabil-
601 ity of Gulf Stream warm-core rings in response to the North Atlantic Oscillation.
602 *Continental Shelf Research*, 29(7), 856–869. doi: 10.1016/j.csr.2009.01.008
- 603 Chelton, D. B., A. d. R., Schlax, M. G., Naggar, K., & Siwetz, N. (1998). Geo-
604 graphical variability of the first baroclinic Rossby radius of deformation. *Journal*
605 *of Physical Oceanography*, 28(3), 433–460. doi: 10.1175/1520-0485(1998)028<433:
606 GVOTFB>2.0.CO;2
- 607 Chelton, D. B., Gaube, P., Schlax, M. G., Early, J. J., & Samelson, R. M. (2011).
608 The influence of nonlinear mesoscale eddies on near-surface oceanic chlorophyll.
609 *Science*, 334(6054), 328–32. doi: 10.1126/science.1208897
- 610 Chelton, D. B., & Schlax, M. G. (2013). *Mesoscale eddies in altimeter observations*
611 *of ssh*.
- 612 Chelton, D. B., Schlax, M. G., Samelson, R. M., & de Szoeke, R. A. (2007). Global
613 observations of large oceanic eddies. *Geophysical Research Letters*, 34(15),
614 L15606. doi: 10.1029/2007GL030812
- 615 CMEMS. (2017). The Ssalto/Duacs altimeter products were produced and dis-
616 tributed by the Copernicus Marine and Environment Monitoring Service. *Aviso*
617 *Dataset*. Retrieved from <https://www.aviso.altimetry.fr/>
- 618 Cui, W., Wang, W., Zhang, J., & Yang, J. (2020). Identification and census statis-
619 tics of multicore eddies based on sea surface height data in global oceans. *Acta*
620 *Oceanologica Sinica*, 39(1), 41–51. doi: 10.1007/s13131-019-1519-y
- 621 Faghmous, J. H., Frenger, I., Yao, Y., Warmka, R., Lindell, A., & Kumar, V. (2015,
622 6). A daily global mesoscale ocean eddy dataset from satellite altimetry. *Scientific*

- 623 *Data*, 2, 150028 EP -. doi: 10.1038/sdata.2015.28
- 624 Ferrari, R., & Wunsch, C. (2009). Ocean Circulation Kinetic Energy: Reservoirs,
625 Sources, and Sinks. *Annual Review of Fluid Mechanics*, 41(1), 253–282. doi: 10
626 .1146/annurev.fluid.40.111406.102139
- 627 Frenger, I., Gruber, N., Knutti, R., & Münnich, M. (2013). Imprint of Southern
628 Ocean eddies on winds, clouds and rainfall. *Nature Geoscience*, 6(8), 608 EP -.
629 doi: 10.1038/ngeo1863
- 630 Frenger, I., Münnich, M., Gruber, N., & Knutti, R. (2015). Southern Ocean eddy
631 phenomenology. *Journal of Geophysical Research: Oceans*, 120(11), 7413-7449.
632 doi: 10.1002/2015JC011047
- 633 Fu, L., Chelton, D., Le Traon, P., & Oceanography, M. R. (2010). Eddy dynamics
634 from satellite altimetry. *Oceanography*, 23(4), 14-25. doi: 10.2307/24860859
- 635 Gill, A., Green, J., & Simmons, A. (1974). Energy partition in the large-scale ocean
636 circulation and the production of mid-ocean eddies. *Deep Sea Res Oceanogr Abstr*,
637 21(7), 499-528. doi: 10.1016/0011-7471(74)90010-2
- 638 Hogg, A. M., & Blundell, J. R. (2006). Interdecadal variability of the southern
639 ocean. *Journal of Physical Oceanography*, 36(8), 1626-1645. doi: 10.1175/
640 JPO2934.1
- 641 Hogg, A. M., Meredith, M. P., Chambers, D. P., Abrahamsen, E. P., Hughes,
642 C. W., & Morrison, A. K. (2015). Recent trends in the Southern Ocean
643 eddy field. *Journal of Geophysical Research: Oceans*, 120(1), 257-267. doi:
644 10.1002/2014JC010470
- 645 Hu, S., Sprintall, J., Guan, C., McPhaden, M. J., Wang, F., Hu, D., & Cai,
646 W. (2020, 2). Deep-reaching acceleration of global mean ocean circula-
647 tion over the past two decades. *Science Advances*, 6(6), eaax7727. doi:
648 10.1126/sciadv.aax7727
- 649 Japan Meteorological Agency, Japan. (2013). *Jra-55: Japanese 55-year reanalysis,*
650 *daily 3-hourly and 6-hourly data*. Boulder CO: Research Data Archive at the Na-
651 tional Center for Atmospheric Research, Computational and Information Systems
652 Laboratory. Retrieved from <https://doi.org/10.5065/D6HH6H41>
- 653 Kang, D., & Curchitser, E. N. (2013). Gulf stream eddy characteristics in a high-
654 resolution ocean model. *Journal of Geophysical Research: Oceans*, 118(9), 4474-
655 4487. Retrieved from <https://agupubs.onlinelibrary.wiley.com/doi/abs/10>

- 656 .1002/jgrc.20318 doi: <https://doi.org/10.1002/jgrc.20318>
- 657 Kang, D., & Curchitser, E. N. (2017). On the Evaluation of Seasonal Variability of
658 the Ocean Kinetic Energy. *Geophysical Research Letters*, 47, 1675-1583. doi: 10
659 .1175/JPO-D-17-0063.1
- 660 Li, G., Cheng, L., Zhu, J., Trenberth, K. E., Mann, M. E., & Abraham, J. P. (2020).
661 Increasing ocean stratification over the past half-century. *Nature Climate Change*,
662 1–8. doi: 10.1038/s41558-020-00918-2
- 663 Martínez-Moreno, J., Hogg, A. M., England, M., Constantinou, N. C., Kiss, A. E.,
664 & Morrison, A. K. (2021). Global changes in oceanic mesoscale currents over the
665 satellite altimetry record. *Journal of Advances in Modeling Earth Systems*, 0(ja).
666 doi: 10.1029/2019MS001769
- 667 Martínez-Moreno, J., Hogg, A. M., Kiss, A. E., Constantinou, N. C., & Morrison,
668 A. K. (2019). Kinetic energy of eddy-like features from sea surface altimetry.
669 *Journal of Advances in Modeling Earth Systems*, 11(10), 3090-3105. doi:
670 10.1029/2019MS001769
- 671 Patel, R. S., Llort, J., Strutton, P. G., Phillips, H. E., Moreau, S., Pardo, P. C.,
672 & Lenton, A. (2020). The Biogeochemical Structure of Southern Ocean
673 Mesoscale Eddies. *Journal of Geophysical Research: Oceans*, 125(8). doi:
674 10.1029/2020jc016115
- 675 Pilo, G. S., Mata, M. M., & Azevedo, J. L. L. (2015). Eddy surface properties and
676 propagation at Southern Hemisphere western boundary current systems. *Ocean
677 Science*, 11(4), 629–641. doi: 10.5194/os-11-629-2015
- 678 Qiu, B. (1999). Seasonal Eddy Field Modulation of the North Pacific Subtropical
679 Countercurrent: TOPEX/Poseidon Observations and Theory. *Journal of Physical
680 Oceanography*, 29(10), 2471–2486. doi: 10.1175/1520-0485(1999)029<2471:sefmot>2
681 .0.co;2
- 682 Qiu, B., & Chen, S. (2004). Seasonal Modulations in the Eddy Field of the South
683 Pacific Ocean. *Journal of Physical Oceanography*, 34(7), 1515–1527. doi: 10.1175/
684 1520-0485(2004)034<1515:smitef>2.0.co;2
- 685 Qiu, B., Chen, S., Klein, P., Sasaki, H., & Sasai, Y. (2014). Seasonal Mesoscale
686 and Submesoscale Eddy Variability along the North Pacific Subtropical Coun-
687 tercurrent. *Journal of Physical Oceanography*, 44(12), 3079–3098. doi:
688 10.1175/JPO-D-14-0071.1

- 689 Ruela, R., Sousa, M. C., deCastro, M., & Dias, J. M. (2020). Global and regional
690 evolution of sea surface temperature under climate change. *Global and Planetary*
691 *Change*, 190, 103190. doi: 10.1016/j.gloplacha.2020.103190
- 692 Sasaki, H., Klein, P., Qiu, B., & Sasai, Y. (2014). Impact of oceanic-scale inter-
693 actions on the seasonal modulation of ocean dynamics by the atmosphere. *Nature*
694 *Communications*, 5(1), 5636. doi: 10.1038/ncomms6636
- 695 Schubert, R., Schwarzkopf, F. U., Baschek, B., & Biastoch, A. (2019). Submesoscale
696 Impacts on Mesoscale Agulhas Dynamics. *Journal of Advances in Modeling Earth*
697 *Systems*, 11(8), 2745–2767. doi: 10.1029/2019ms001724
- 698 Siegel, D., Peterson, P., DJ, M., Maritorena, S., & Nelson, N. (2011). Bio-optical
699 footprints created by mesoscale eddies in the Sargasso Sea. *Geophysical Research*
700 *Letters*, 38(13), n/a-n/a. doi: 10.1029/2011GL047660
- 701 Uchida, T., Abernathey, R., & Smith, S. (2017). Seasonality of eddy kinetic energy
702 in an eddy permitting global climate model. *Ocean Modelling*, 118, 41-58. doi: 10
703 .1016/j.ocemod.2017.08.006
- 704 Wunsch, C. (2020). Is The Ocean Speeding Up? Ocean Surface Energy Trends.
705 *Journal of Physical Oceanography*, 50(11), 1–45. doi: 10.1175/jpo-d-20-0082.1
- 706 Wunsch, C., & Ferrari, R. (2004). Vertical mixing, energy, and the general circula-
707 tion of the oceans. *Annual Review of Fluid Mechanics*, 36(1), 281–314. doi: 10
708 .1146/annurev.fluid.36.050802.122121
- 709 Wyrtki, K., Magaard, L., & Hager, J. (1976). Eddy energy in the oceans. *Journal of*
710 *Geophysical Research*, 81(15), 2641-2646. doi: 10.1029/JC081i015p02641
- 711 Yue, S., & Wang, C. (2004). The Mann-Kendall Test Modified by Effective Sample
712 Size to Detect Trend in Serially Correlated Hydrological Series. *Water Resources*
713 *Management*, 18(3), 201–218. doi: 10.1023/b:warm.0000043140.61082.60
- 714 Zamudio, L., Hurlburt, H. E., Metzger, E. J., Morey, S. L., O'Brien, J. J., Tilburg,
715 C., & Zavala-Hidalgo, J. (2006). Interannual variability of Tehuantepec ed-
716 dies. *Journal of Geophysical Research: Oceans (1978–2012)*, 111(C5). doi:
717 10.1029/2005JC003182